Relevant efficiency enhancement of emerging Cu_2MnSnS_4 thin film solar cells by low temperature annealing

A. Le Donne[1*], S. Marchionna[2], M. Acciarri[1], F. Cernuschi[2] and S. Binetti[1]

[1] Dept. of Materials Science and Solar Energy Research Center (MIB-SOLAR),University of Milano-Bicocca, Via Cozzi 55, Milan (Italy)

[2] RSE SpA, Via R. Rubattino 54, Milan (Italy)

*Corresponding author; email: alessia.ledonne@mater.unimib.it

Abstract

Earth abundant and low cost Cu_2MnSnS_4 (CMTS) thin films were grown by a two-step vacuum approach: metal precursor stacks grown by thermal evaporation were heat treated in elemental sulfur vapors. Cu-poor/Mn-rich CMTS samples with large grain size and good layer compactness were obtained by sulfurization at 585°C with an initial step at 115°C to enhance the metal intermixing. They were primarily tested by Energy Dispersive Spectroscopy, micro-Raman and Photoluminescence. Then, solar cells based on them were realized and tested, showing enhanced performance with respect to a previous study (efficiency 0.5%, open-circuit voltage 302 mV, short-circuit current density 4.6 mA/cm^2, fill factor 36%). A 40 min post-deposition annealing in air at 225°C significantly improved the performance of these emerging PV devices (efficiency 0.83%, open-circuit voltage 354 mV, short-circuit current density 5.8 mA/cm^2, fill factor 40%). The beneficial effects of the low temperature annealing were investigated, in terms both of material properties and PV device performance modification.

Keywords Cu_2MnSnS_4, Earth-abundant, Thin film solar cells, Post-deposition annealing

Introduction

As it is well known, in the last five years thin film solar cell manufacturers strongly suffered from the abrupt decrease of Si module price well below 1$/W$_p$ (Bermudez, 2017). The attention of the research activity on thin film photovoltaics (PV) was therefore even more focused on high efficiency or very low cost materials. Despite the present efficiency of Cu(In, Ga)Se$_2$ (CIGS) thin film solar cells is almost comparable to the well established PV technology based on silicon (Jackson et al., 2011, Poncelet et al., 2017), the low availability in the Earth crust of Indium and Gallium will lead to a progressive increase of their cost, which is expected to constrain terawatt range applications of CIGS-based PV devices (Tao et al., 2011). An attractive alternative for the synthesis of In and Ga free terawatt-scale chalcogenides relies on I$_2$-II-IV-VI$_4$ species, such as copper zinc tin sulfide (CZTS), copper zinc tin selenide (CZTSe) and the sulfur-selenium alloy (CZTSSe) (Suryawanshi et al., 2013, Tombolato et al., 2015). A further compound belonging to this class of materials is copper manganese tin sulfide (CMTS), a p-type semiconductor fully based on Earth-abundant and low-cost elements. As a matter of fact, since Mn is definitely cheaper than Zn, optimized CMTS could potentially provide W$_p$ cost definitely lower than CZTS, which is crucial for thin film PV applications (Marchionna et al., 2017). CMTS, which crystallizes into a stannite structure (space group: I-42m), shows high absorption coefficient ($\cong 10^4$ cm^{-1}) and direct band gap (Liang et al., 2012 and Cui et al., 2012) suitable for PV applications. So far, CMTS was mainly studied as magnetic semiconductor in the form of single crystal or nanocrystal (Liang et al., 2012, Cui et al., 2012, Fries et al., 1997 and Podsiadlo et al. 2015), while, very recently, few papers reported on CMTS thin films for PV applications (Marchionna et al., 2017, Chen et al., 2015a, Chen et al., 2015b and Chen et al., 2016). In (Chen et al., 2015a) the synthesis and properties of CMTS layers prepared by direct liquid coating followed by annealing in nitrogen atmosphere were described, which were used in (Chen et al., 2015b) as PV absorbers in solar cells with 0.49% maximum efficiency. Some of the same authors reported also on CMTS PV absorbers prepared by

direct liquid coating followed both by annealing in nitrogen atmosphere and post-sulfurization in sulfur vapors, reaching a 0.38% maximum efficiency (Chen et al., 2016).

In this work, CMTS thin films were grown by a two-step process, whose first optimization is reported in (Marchionna et al., 2017). Metal precursor stacks grown by thermal evaporation are annealed in non toxic sulfur vapors. As it is widely known, this deposition approach led to record efficiency both in CIGS (Jackson et al., 2011) and pure sulfide CZTS (Shin et al., 2013). Of the many possible stoichiometries, Cu-poor/Mn-rich CMTS films with Mn/Sn ratio around 1 were chosen in order to prevent the development of both highly conductive (e.g. $Cu_{2-x}S$) and insulating (e.g. MnS) secondary phases. The grown CMTS thin films were tested by Energy Dispersive Spectroscopy, Raman and Photoluminescence, then some solar devices were manufactured and tested, as described in the following. Considering the beneficial effects of low temperature post-deposition annealing either in air or inert atmosphere recently reported in the literature for kesterite based solar cells (Neuschitzer et al., 2015 and Jiang et al., 2016), the effect of thermal treatments between 200 and 275°C on CMTS solar cell efficiency was investigated, both in terms of electrical performance and modification of the material properties. The results are reported and discussed.

Experimental

CMTS thin films with approximate final thickness around 1.5 μm (measured by a Veeco-Dektak 150 profilometer) were grown by a two step process. Metal precursors were deposited by thermal evaporation on 4x4 cm^2 Mo coated soda lime glasses (SLG) in the sequence SLG/Mo/Sn(235 nm)/Cu(176 nm)/Mn(135 nm). The Mo back contact deposited by DC magnetron sputtering was 1 μm thick. All metal precursor layers have been deposited by a 4-sources electron beam (EB) evaporation system (Kurt J. Lesker PVD 75) in a high vacuum chamber with $2x10^{-7}$ mbar base pressure. Both Sn and Cu beads were evaporated with deposition rates of 2.5 Å/sec and 1.5 Å/sec, respectively, while Mn powders were evaporated at 3 Å/sec.

CMTS thin films were then formed by thermal treatment of the metal precursors in sulfur vapors. Such a sulfurization process was performed in a tube furnace, where the stack of metal precursors and a quartz crucible with 0.3 g of sulfur were loaded in the same quartz boat. The metal precursors were then annealed at 585°C in a mixed argon (50 cm^3/min flux) and elemental sulfur atmosphere for 60 min (ramping rate of 15 °C/min), with an additional initial step at 115°C for 60 min, to enhance the metal intermixing.

Both morphology and chemical composition of the CMTS layers were investigated by a MIRA3 Tescan Scanning Electron Microscope (SEM) equipped for Energy-Dispersive Spectroscopy (EDS). The operating voltage used for all the SEM images was 20 kV, while EDS analyses were performed by a Quantax system (Bruker) under the following conditions: operating voltage 20 kV, probe current 150 pA, probe size 5 nm, working distance 15 mm, with inner-calibration on pure metals.

The crystal structure of the CMTS films was examined by Raman spectroscopy. Raman measurements were carried out at room temperature by a Jasco Ventuno micro-Raman system in backscattering configuration, equipped with a Peltier-cooled charge-coupled device camera (operating temperature: -50°C) and a He-Ne laser (excitation wavelength: 632.8 nm). Raman spectra were calibrated before each measurement by imposing the position of the dominant peak of a monocrystalline Si reference at 520.65 cm^{-1}. Proper laser power density was chosen to generate the best signal-to-noise ratio without broadening or shifting the Raman peaks due to local heating. In particular, a 20X-0.46 NA objective providing a spot diameter of 4 μm and a laser power of 0.8 mW were used.

Photoluminescence (PL) spectra were recorded both in the 450-800 nm and in the 850-1700 nm spectral range. PL measurements in the visible range were performed with a spectral resolution of 5 nm by a Fluorolog 3.21 spectrometer provided by Jobin Yvon. The excitation source consists of a 450 W Xe lamp coupled with a 1200 grooves/mm double grating monochromator. The signal detection equipment consists of a 1200 grooves/mm single grating monochromator and of a phototube detector (Hamamatsu R928P). A cooling system consisting of rotary pump, diffusion

pump, l-N_2 cold trap and Cryomech PT405 cryorefrigerator was used to perform PL measurements at low temperature up to 7 K. As far as analyses in the IR range are concerned, PL measurements were performed with a spectral resolution of 6.6 nm using a standard lock-in technique in conjunction with a single grating monochromator and a short wavelength enhanced InGaAs detector with maximum responsivity at 1540 nm. A quantum well laser (λ_{exc}=805 nm) was mainly used as excitation source, along with a 532 nm laser sometimes employed for comparison purposes. A cooling system consisting of rotary pump, turbomolecular pump and He closed circuit cryostat was used to perform PL measurements at low temperature up to 15 K.

CMTS solar cells with an active area of 0.15 cm^2 were then obtained as reported in (Marchionna et al., 2017).

Post-deposition thermal treatments in air or Argon atmosphere at 200, 225, 250 and 275°C for 10 to 120 min were finally tested to investigate the effect of low temperature annealing on CMTS solar cell efficiency. Despite in the literature hot plates in open air were usually employed to this purpose (Neuschitzer et al., 2015 and Jiang et al., 2016), in this work a pre-heated lab drying oven was preferred to perform thermal treatments in air. In fact, lab drying ovens provide homogeneous heating and ensure temperature stability and reproducibility, thus minimizing the time needed to heat the CMTS solar cells up to the chosen temperature. Annealing in Argon atmosphere was instead performed using a quartz tube and a pre-heated tube furnace. In both cases, the samples were removed from the pre-heated environment at the end of the annealing time and cooled down to room temperature in a couple of minutes.

The CMTS devices were inspected both by External Quantum Efficiency and current density-voltage (J-V) measurements before and after each annealing. External Quantum Efficiency (EQE) measurements were obtained by a SpeQuest quantum efficiency system. The PV devices were illuminated by a chopped light beam with a diameter around 3 mm. The photogenerated current from the cell passed through an I-V converter and the corresponding voltage produced at each wavelength of the monochromatic light was measured by a lock-in amplifier monitored via PC. The

spectral response curves of the PV device were taken from 350 nm to 1200 nm with a 10 nm wavelength increment. The EQE spectrum was then calculated as the ratio between the spectral response data and the incident light spectrum, obtained by a reference photodiode (ThorLabs S120VC). J-V measurements under 1 Sun illumination (100 mW/cm^2) in Air Mass 1.5G conditions were recorded by a Thermo Oriel Solar simulator.

Results and discussion

As pointed out in (Marchionna et al., 2017), the strict control of the Mn deposition rate is a critical issue, since in the selected operative conditions Mn sublimates at very low EB current. Despite in (Marchionna et al., 2017) SLG/Mo/Mn/Sn/Cu/Mn stack structures led to the best CMTS morphology, in this work metal precursors were grown in the sequence SLG/Mo/Sn/Cu/Mn. As a matter of fact, a two-step Mn evaporation increases the error on the total Mn thickness, which in turn negatively affects both the sample reproducibility and the solar cell performance due to a higher content of the $Cu_{7.38(11)}Mn_4Sn_{12}S_{32}$ insulating secondary phase, as demonstrated in (Marchionna et al., 2017). Furthermore, Mn powders were used for the Mn evaporation, as an alternative to the Mn flakes employed in (Marchionna et al., 2017), which also enhanced the control on the final Mn layer thickness. The effectiveness of these simple modifications to the previous optimization (Marchionna et al., 2017) is proven first of all by EDS analyses performed at different magnifications, which showed a very good homogeneity of the Mn/Sn ratio over a wide range of inspected regions (see Table 1). A further confirmation is given by J-V analyses under 1 sun illumination (see Fig. 1), which showed not only enhanced solar cell parameters with respect to (Marchionna et al., 2017) (efficiency 0.5% vs 0.33%, open-circuit voltage 302 vs 226 mV, short-circuit current density 4.6 vs 4 mA/cm^2, fill factor 36% vs 36.3%), but also a good homogeneity of the device performance over a 4x2 cm^2 area. As expected, the overall material properties are in total agreement with (Marchionna et al., 2017), since no other growth parameters have been modified.

As an example, Fig. 2 confirms that large grain size and good layer compactness were obtained, in agreement with (Marchionna et al., 2017).

The above described CMTS/CdS/iZnO+AZO heterostructures (i.e. the full cell) were submitted to 10 min annealing in air at 200, 225, 250 and 275°C. As shown in Figure 3, for all the selected temperatures no improvements were obtained, therefore longer annealing times between 20 and 120 min with 20 min step were tested. The results (see Fig. 3) demonstrated that for all the tested temperatures an almost linear efficiency increase is observed up to 40 min, while for longer annealing times a gradual performance deterioration occurs.

The evolution of all device parameters with temperature for 40 min annealing in air is shown in detail in Figure 4. It should be remarked that 40 min post-deposition thermal treatments have been tested only on the full cell, since it was demonstrated in (Neuschitzer et al., 2015) that CdS layers not protected by i-ZnO+AZO start deteriorating at similar temperatures for annealing times longer than 20 min. As shown in Fig. 4, in spite the best V_{oc} and J_{sc} increases are associated to thermal treatments at 250°C and 200°C, respectively, the only annealing at 225°C allows for an improvement of all the device parameters, which led to a 0.83% efficiency (see Fig. 5(a)). Less pronounced enhancements were obtained instead for 40 min annealing at 225°C in Argon atmosphere. As shown in Fig. 4, inert atmosphere promotes the increase of FF, while inducing less pronounced improvements of both V_{oc} and J_{sc}, suggesting that oxygen may be partially involved in the beneficial device modifications. However, further investigations are needed to shed light on this evidence.

Dark J-V curves of CMTS solar cell before and after 40 min annealing at 225°C in air are shown in Fig. 5(b). Ideality factors (n) and saturation current densities (J_0) were obtained by fitting the dark J-V curves with a standard single diode model. As expected from the results reported in Figs. 4 and 5(a), the annealed device shows relatively low n and J_0 values (4 and 39 $\mu A/cm^2$) with respect to those before any annealing (5 and 170 $\mu A/cm^2$), due to its better electrical rectification in the forward applied bias region. The n and J_0 reduction for the annealed device also implies a

successful decrease in series resistance (R_s) along with an increase of the shunt resistance (R_{sh}) after low-temperature annealing (see Fig. 5(b)), leading to improvements of J_{SC} and FF.

The results reported in Fig. 4 are confirmed by EQE analyses (see Fig. 6), which show a significant increase of the spectral response between 550 and 800 nm for all the tested temperatures, indicating a reduction of recombination losses. Meanwhile, a gradual decrease of EQE is observed between 350 and 500 nm, suggesting an increase of CdS absorption. In agreement with J-V analyses, CMTS solar cells annealed at 250°C and 200°C show, respectively, the highest reduction of recombination losses (i.e. best V_{oc} increase) and the lowest increase of CdS absorption (i.e. best J_{sc} increase). Annealing at 225°C lead to a significant reduction of recombination losses without a strong increase of CdS absorption, allowing therefore for the best overall performance enhancement.

The reasons behind these beneficial modifications of the device parameters were investigated by Raman and PL spectroscopies. In agreement with (Marchionna et al., 2017), Figure 7 shows the characteristic Raman modes of the CMTS phase at 250, 282, 302, 330, 350 and 364 cm^{-1} (Podsiadlo et al., 2015 and Himmrich and Haeuseler, 1991), along with a small peak at 164 cm^{-1} related to SnS (Raadik et al., 2013), suggesting that no modifications occur upon annealing between 200 and 275°C. PL analyses both in the infrared and in the visible range provided instead a deeper insight on the origin of the performance enhancement. As depicted by the black curve in Fig. 8(a), before any annealing, CMTS solar cells show the same PL features reported in (Marchionna et al., 2017), that is a broad band at about 0.8 eV, most probably related to a deep recombination center, and a less intense band at about 1.2 eV. In our previous work (Marchionna et al., 2017), the band at about 1.2 eV was attributed to band-edge recombination due to the close agreement with the energy gap (E_g) value determined by transmittance measurements. However, a careful consideration of the EQE curves reported in Fig. 6 raised some doubts on that E_g value. In fact, in spite the E_g determination from EQE curves with significant recombination losses is difficult due to the low signal in the long wavelength region (Neuschitzer et al., 2015), Fig. 6 suggests energy gap values around 1.5 eV. Most probably this is connected to the presence of secondary phases in the considered CMTS films:

the SnS phase detected by Raman spectroscopy (see Fig. 7) shows E_g around 1.3 eV (Koteswara Reddy et al., 1998), while the energy gap of the spinel phase $Cu_{7.38(11)}Mn_4Sn_{12}S_{32}$ detected by X ray diffraction on similar CMTS samples (Marchionna et al., 2017) is unknown, however its color is black. A most reliable attribution of the band at 1.2 eV involves therefore a radiative recombination associated to defect related levels in the bandgap, as in the case of CZTS (Leitao et al., 2011, Romero et al., 2011, Gershon et al., 2013 and Le Donne et al., 2015).

The comparison of the black curve (λ_{exc}= 805 nm) in Fig. 8(a) with PL excited by a laser with lower penetration depth in CMTS (λ_{exc}= 532 nm, see grey curve in Fig. 8(a)) demonstrates that the deep recombination center responsible for the emission at 0.8 eV is associated to a bulk defect. As shown in Fig. 8(b), the intensity of the band at 0.8 eV starts decreasing upon thermal treatment at 200°C, until disappearing in solar cells annealed at 250 and 275°C, where the band at 1.2 eV dominates. This suggests that low-temperature annealing generally reduces the density of the deep bulk defect responsible for the emission at 0.8 eV, thus reducing recombination losses. This reduction of detrimental deep recombination centers after low-temperature annealing explains the n and J_0 lowering deduced from the dark J-V curves in Fig. 5(b), indicating an effective reduction of the recombination current through the Shockley-Read-Hall recombination path. In particular, thermal treatments at 250°C provided the best reduction of detrimental deep recombination centers, thus explaining both the highest V_{oc} improvement and the optimal EQE increase above 550 nm shown in Figs. 4 and 6, respectively.

As far as CdS layer is concerned, Figure 9 shows that, before any annealing, CdS shows a very weak PL emission at about 2.5 eV, which corresponds to the typical energy gap value of nanocrystalline CdS (Park et al., 2009). After 200°C annealing the PL signal increases strongly and shifts to 2.45 eV indicating an improvement of CdS crystalline quality, in agreement with (Neuschitzer et al., 2015). With increasing annealing temperature up to 250°C, CdS crystalline quality keeps increasing as demonstrated both by the further increase of PL intensity and by the reduced energy gap value (i.e. 2.25 eV). The decrease of PL intensity observed instead for 275°C

annealing most probably marks the beginning of CdS deterioration. The modifications of CdS crystalline quality explain very well both J-V and EQE analyses: a 200°C annealing significantly improve the CdS layer quality without a strong decrease of the energy gap value, which shifts from 2.5 to 2.45 eV. Conversely, thermal treatments at higher temperature significantly reduce the energy gap value from 2.5 to 2.25 eV, thus shifting the CdS absorption edge, in agreement with the EQE curves reported in Fig. 6. PL analyses explain therefore why 225°C annealing lead to a significant reduction of recombination losses without a strong increase of CdS absorption, allowing for the best overall performance enhancement.

Conclusions

Earth abundant CMTS thin films were obtained by sulfurization at 115°C+585°C of SLG/Mo/Sn/Cu/Mn stacks grown by thermal evaporation. Cu-poor/Mn-rich CMTS samples with a good homogeneity of the metal compositional ratios were obtained by a strict control of the Mn evaporation rate. Solar cells based on them showed enhanced performance with respect to a previous study (efficiency 0.5% vs 0.33%, open-circuit voltage 302 vs 226 mV, short-circuit current density 4.6 vs 4 mA/cm^2, fill factor 36% vs 36.3%). The effects of post-deposition thermal treatments between 200 and 275°C on the same CMTS PV devices were investigated, both in terms of electrical performance and modification of the material properties. The best annealing in air at 225°C for 40 min allowed for a significant improvement of their performance (efficiency 0.83%, open-circuit voltage 354 mV, short-circuit current density 5.8 mA/cm^2, fill factor 40%), further increasing the efficiency of this promising material.

Acknowledgements

References

Bermudez, 2017 V. Bermudez, Economical and operational issues for CIGS in the future PV panorama, Solar Energy 146 (2017), pp 85–93

Chen et al., 2015a L. Chen, H. Deng, J. Tao, W. Zhou, L. Sun, F. Yue, P. Yang, J. Chu, Influence of annealing temperature on structural and optical properties of Cu_2MnSnS_4 thin films fabricated by sol–gel technique, Journal of Alloys and Compounds, 640 (2015), pp 23-28

Chen et al., 2015b L. Chen, H. Deng, J. Tao, H. Cao, L. Huang, L. Sun, P. Yang, J. Chu, Synthesis and characterization of earth-abundant Cu_2MnSnS_4 thin films using a non-toxic solution based technique, RSC Advances, 5 (2015), pp 84295-84302

Chen et al., 2016 L. Chen, H. Deng, J. Tao, H. Cao, L. Sun, P. Yang, J. Chu, Strategic improvement of Cu_2MnSnS_4 films by two distinct postannealing, Acta Materialia, 109 (2016), pp 1-7

Cui et al., 2012 Y. Cui, R. Deng, G. Wang, D. Pan, A general strategy for synthesis of quaternary semiconductor Cu_2MSnS_4 (M = Co^{2+}, Fe^{2+}, Ni^{2+}, Mn^{2+}) nanocrystals, J. Mater. Chem., 22 (2012), 23136-23140

Fries et al., 1997 T. Fries, Y. Shapira, F. Palacio, M.C. Moron, G.J. McIntyre, R. Kershaw, A. Wold, E.J. McNiff, Magnetic ordering of the antiferromagnet Cu_2MnSnS_4 from magnetization and neutron-scattering measurements, Phys. Rev. B: Condens. Matter, 56 (1997), 5424-5431

Gershon et al. 2013 T. Gershon, B. Shin, T. Gokmen, S. Lu, N. Bojarczuk, and S. Guha, Relationship between Cu_2ZnSnS_4 quasi donor-acceptor pair density and solar cell efficiency, Applied Physics Letters 103(19) (2013) Article ID 193903

Himmrich and Haeuseler, 1991 M. Himmrich, H. Haeuseler, Far infrared studies on stannite and wurtzstannite type compounds, Spectrochim. Acta A, 47 (1991), pp 933-942

Jackson et al., 2011 P. Jackson, D. Hariskos, E. Lotter, S. Paetel, R. Wuerz, R. Menner, W. Wischmann, M. Powalla, New world record efficiency for $Cu(In,Ga)Se_2$ thin-film solar cells beyond 20%, Prog. Photovolt: Res. Appl., 19 (2011), pp 894-897

Jiang et al., 2016 F. Jiang, C. Ozaki, Gunawan, T. Harada, Z. Tang, T. Minemoto, Y. Nose, S. Ikeda, Effect of Indium Doping on Surface Optoelectrical Properties of Cu_2ZnSnS_4 Photoabsorber and Interfacial/Photovoltaic Performance of Cadmium Free In_2S_3/Cu_2ZnSnS_4 Heterojunction Thin Film Solar Cell, Chem. Mater. 28 (2016), pp 3283-3291

Koteswara Reddy et al. 1998 N. Koteswara Reddy, K.T. Ramakrishna Reddy, Growth of polycrystalline SnS films by spray pyrolysis, Thin Solid Films 325 (1998), pp 4–6

Le Donne et al. 2015 A. Le Donne, S. Marchionna, P. Garattini, R. A. Mereu, M. Acciarri and S. Binetti, Effects of CdS Buffer Layers on Photoluminescence Properties of Cu_2ZnSnS_4 Solar Cells, International Journal of Photoenergy 2015 (2015) Article ID 583058

Leitao et al. 2011 J. P. Leitao, N. M. Santos, P. A. Fernandes, P. M. P. Salomé, A. F. da Cunha, J. C. González, G. M. Ribeiro, and F. M. Matinaga, Photoluminescence and electrical study of fluctuating potentials in Cu_2ZnSnS_4-based thin films, Physical Review B 84(2) (2011) Article ID 024120

Liang et al., 2012 X. Liang, P. Guo, G. Wang, R. Deng, D. Pan, X. Wei, Dilute magnetic semiconductor Cu_2MnSnS_4 nanocrystals with a novel zincblende and wurtzite structure, RSC Advances, 2 (2012), pp 5044-5046

Marchionna et al., 2017 S. Marchionna, A. Le Donne, M. Merlini, S. Binetti, M. Acciarri, F. Cernuschi, Growth of Cu_2MnSnS_4 PV absorbers by sulfurization of evaporated precursors, Journal of Alloys and Compounds 693 (2017) 95-102

Neuschitzer et al., 2015 M. Neuschitzer, Y. Sanchez, T. Olar, T. Thersleff, S. Lopez-Marino, F. Oliva, M. Espindola-Rodriguez, H. Xie, M. Placidi, V. Izquierdo-Roca, I. Lauermann, K. Leifer, A.

Pérez-Rodriguez, E. Saucedo, Complex Surface Chemistry of Kesterites: Cu/Zn Reordering after Low Temperature Postdeposition Annealing and Its Role in High Performance Devices, Chem. Mater., 27 (2015), pp 5279-5287

Park et al., 2009 K. Park, H.J. Yu, W.K. Chung, B.J. Kim, S.H. Kim, Effect of heat-treatment on CdS and CdS/ZnS nanoparticles, J. Mater. Sci., 44 (2009), pp 4315-4320

Podsiadlo et al., 2015 S. Podsiadlo, M. Bialoglowski, M. Fadaghi, W. Gebicki, C. Jastrzebski, E. Zero, D. Trzybinski, K. Wozniak, Synthesis of magnetic doped kesterite single crystals, Cryst. Res. Technol., 50 (9-10) (2015), pp 690-694

Poncelet et al., 2017 O. Poncelet, R. Kotipalli, B. Vermang, A. Macleod, L.A. Francis, D. Flandre, Optimisation of rear reflectance in ultra-thin CIGS solar cells towards >20% efficiency, Solar Energy 146 (2017), pp 443–452

Raadik et al., 2013 T. Raadik, M. Grossberg, J. Raudoja, R. Traksmaa, J. Krustok, Temperature-dependent photoreflectance of SnS crystals, J.Phys.Chem.Sol.,74(12) (2013), pp 1683-1685

Romero et al. 2011 M. J. Romero, H. Du, G. Teeter, Y. Yan, and M. M. Al-Jassim, Comparative study of the luminescence and intrinsic point defects in the kesterite Cu_2ZnSnS_4 and chalcopyrite $Cu(In,Ga)Se_2$ thin films used in photovoltaic applications, Physical Review B 84(16) (2011) Article ID 165324

Shin et al., 2013 B. Shin, O. Gunawan, Y. Z. Nestor, A. Bojarczuk, S. Jay Chey, S. Guha, Thin film solar cell with 8.4% power conversion efficiency using an earth-abundant Cu_2ZnSnS_4 absorber, Prog. Photovolt. Res. Appl., 21(1) (2013), pp 72-76

Suryawanshi et al., 2013 M. P. Suryawanshi, G. L. Agawane, S. M. Bhosale, S. W. Shin, P. S. Patil, J. H. Kim and A. V. Moholkar, CZTS based thin film solar cells: A status review, Materials Technology, 28 (2013), pp 98-109

Tao et al., 2011 C.S. Tao, J. Jiang, M. Tao, Natural resource limitations to terawatt-scale solar cells, Solar Energy Materials and Solar Cells, 95 (2011), pp 3176-3180

Tombolato et al., 2015 S. Tombolato, U. Berner, D. Colombara, D. Chrastina, M. Widenmeyer, S.O. Binetti, P.J. Dale, Cu2ZnSnSe4 device obtained by formate chemistry for metallic precursor layer fabrication, Solar Energy 116 (2015), pp 287–292

Figures

	1kx	**15kx**	**30kx**	**50kx**
Sulfur (at.%)	53.5	54.2	55.9	52.9
Tin (at.%)	12.7	12.3	11.5	12.8
Copper (at.%)	21.0	21.1	20.1	21.8
Manganese (at.%)	12.8	12.4	12.5	12.4
Mn/Sn	1.0	1.0	1.1	1.0
Cu/Sn+Mn	0.8	0.9	0.8	0.9

Table 1. EDS analyses performed at different magnifications on CMTS samples obtained by sulfurization of SLG/Mo/Sn/Cu/Mn stacks at 115+585°C.
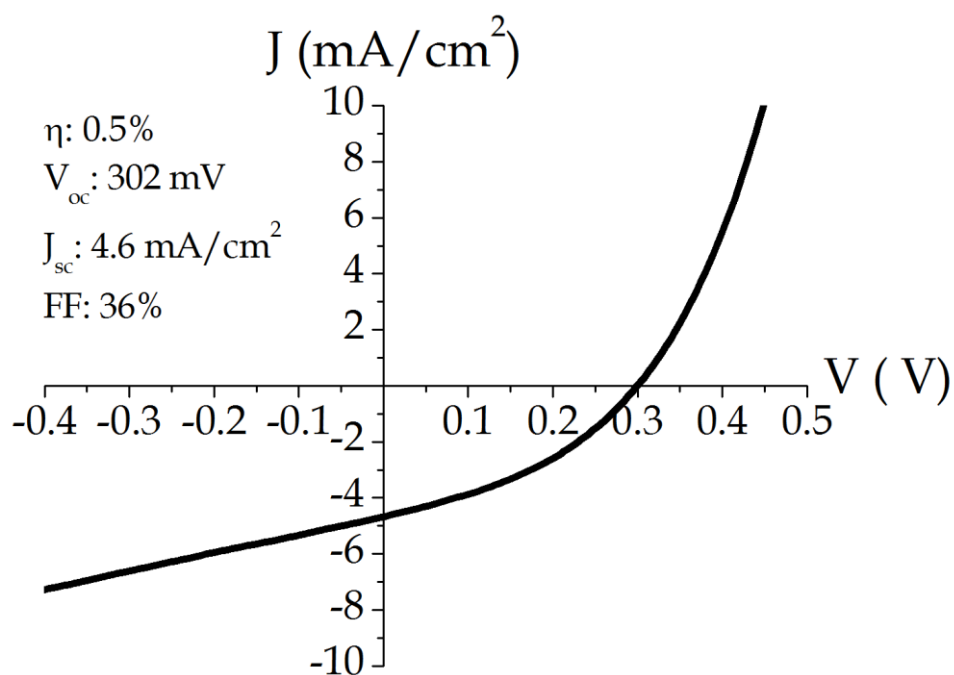
Figure 1. J-V curve under 1 sun illumination performed on CMTS samples obtained by sulfurization of SLG/Mo/Sn/Cu/Mn stacks at 115+585°C.
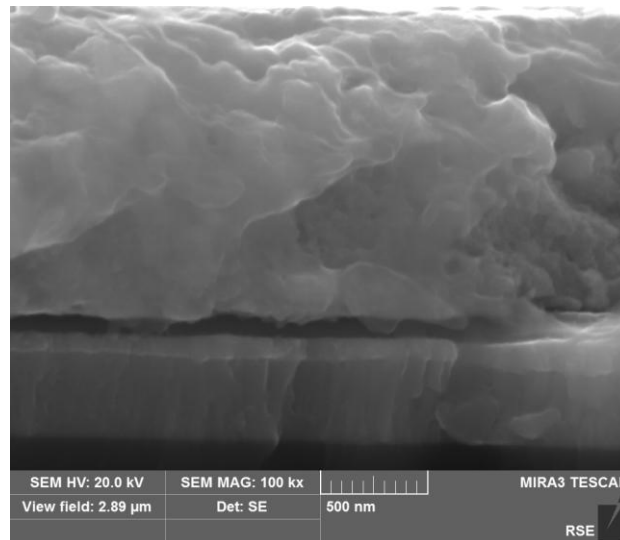
Figure 2. Cross sectional SEM image of a typical CMTS sample grown by sulfurization of the SLG/Mo/Sn/Cu/Mn stack structure at 115+585°C.
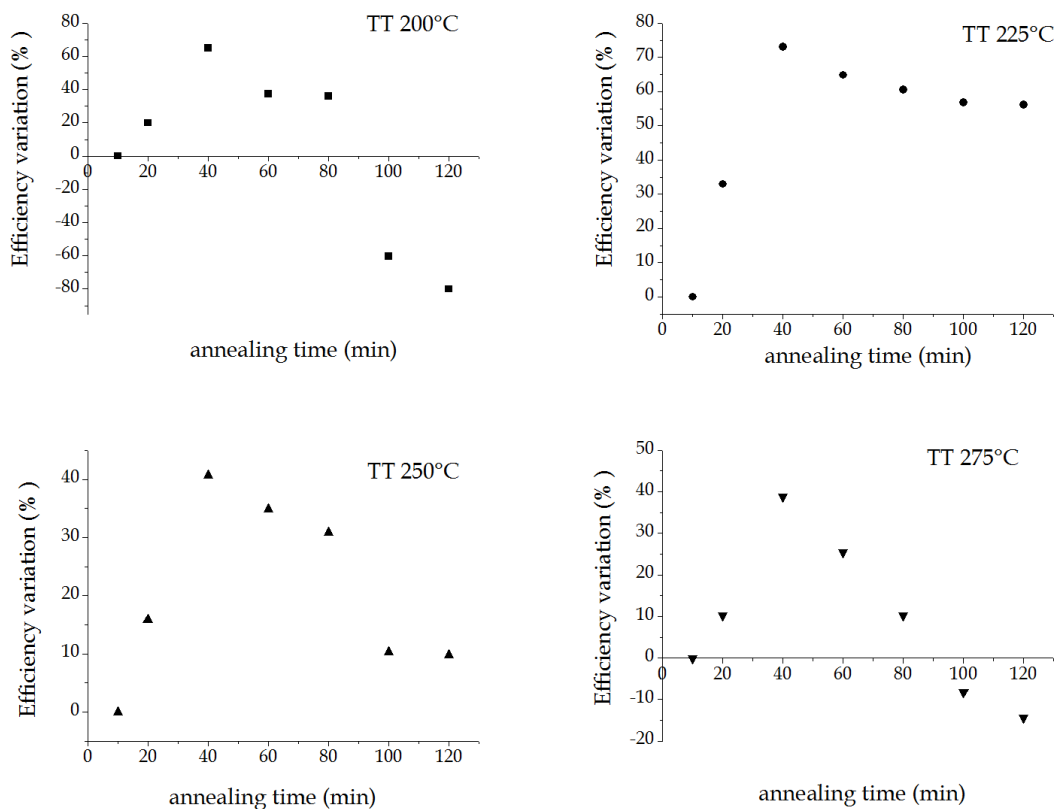
Figure 3. Percentage variation of the device efficiency after post-deposition annealing between 200 and 275°C in air as a function of the annealing time.
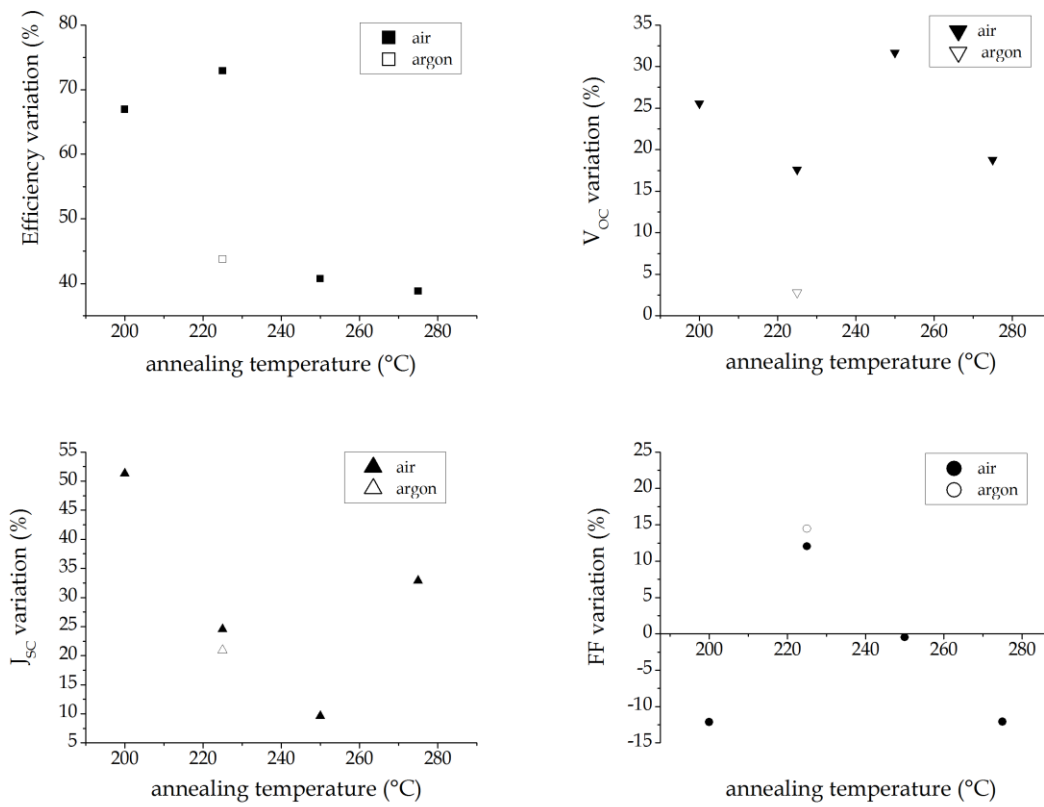
Figure 4. Percentage variation of the device performance after 40 min post-deposition annealing in air or Argon atmosphere as a function of the annealing temperature.
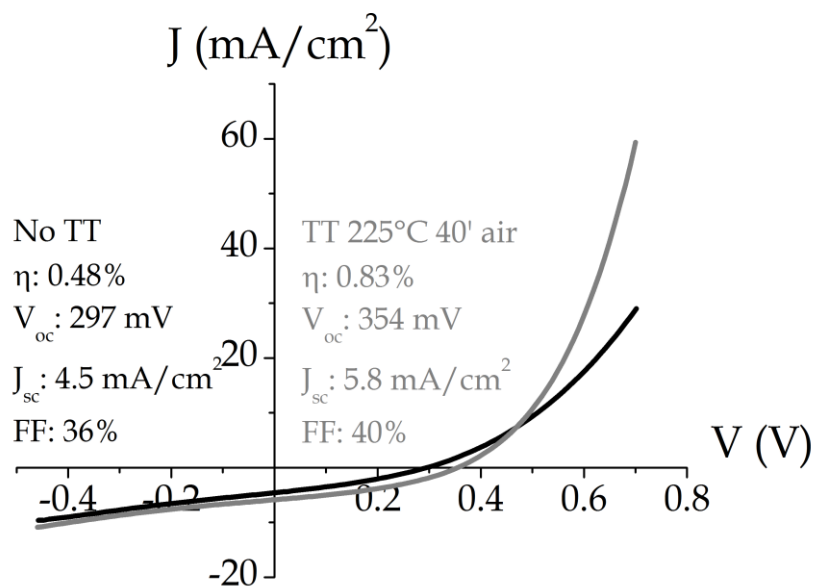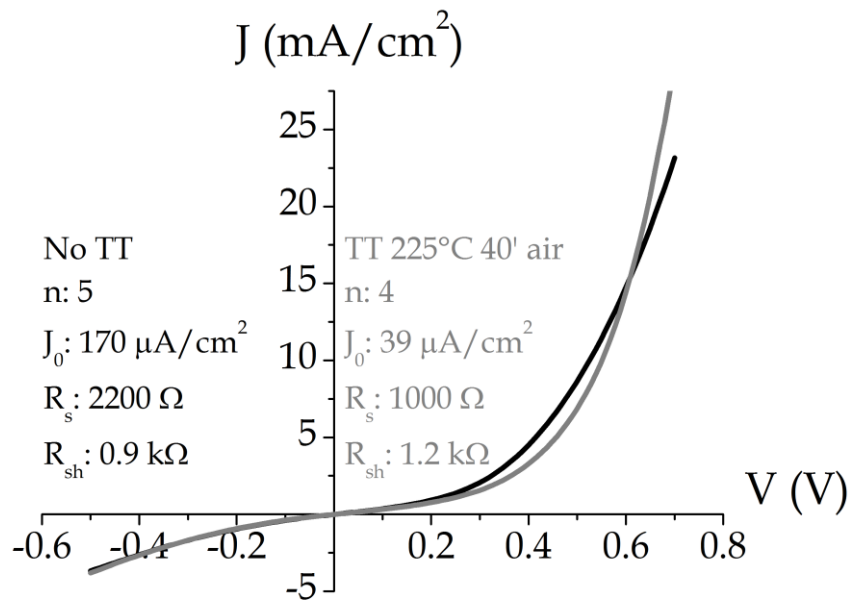
Figure 5. J-V curves before and after a 40 min post-deposition annealing at 225°C in air. (a) J-V curves under AM1.5G illumination; (b) dark J-V curves.
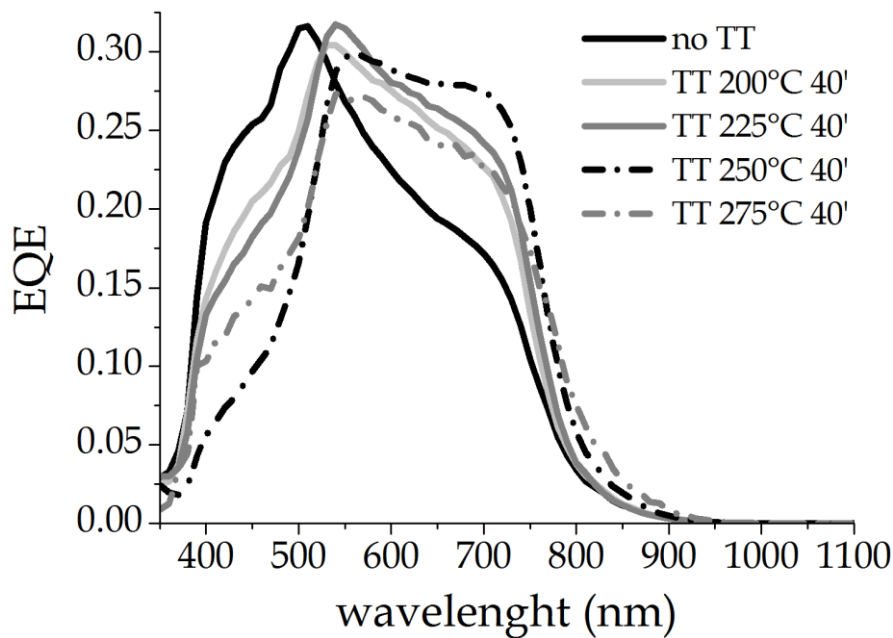
Figure 6. External quantum efficiency curves before and after 40 min post-deposition thermal treatments (labeled as TT) in air as a function of the annealing temperature.
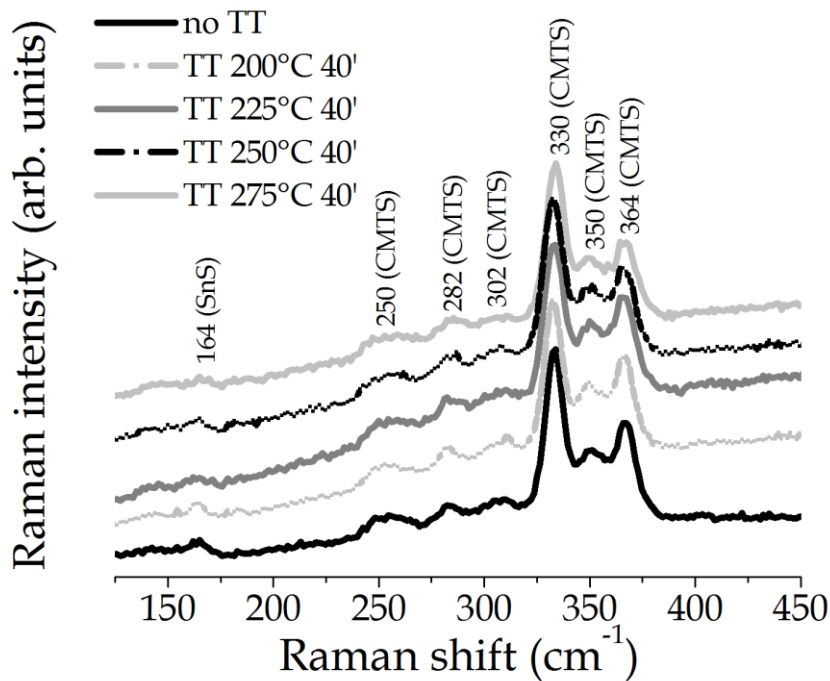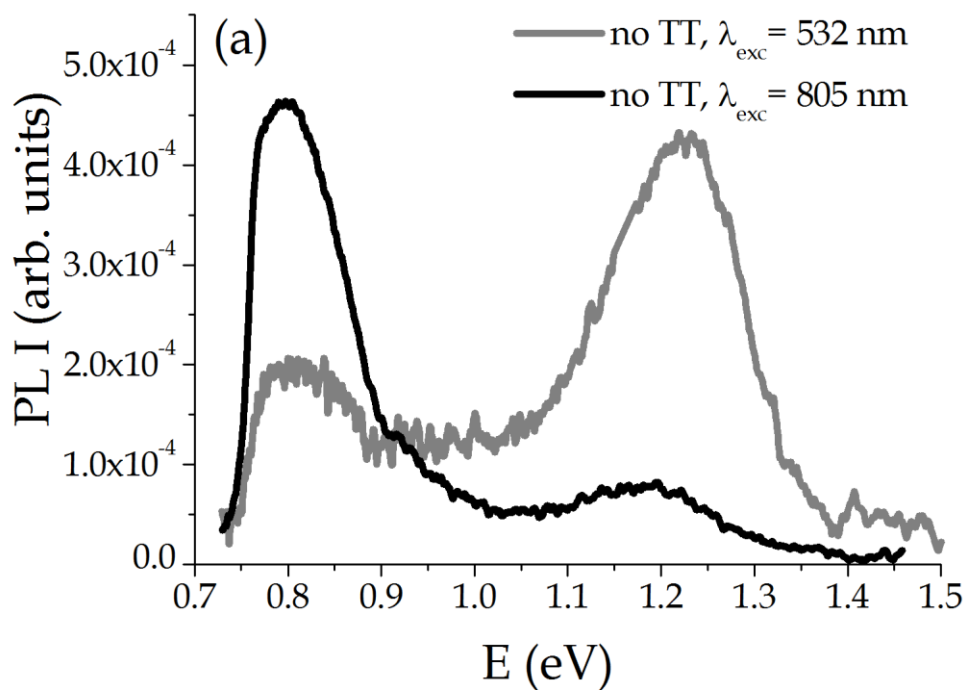
Figure 7. Raman spectra before and after 40 min post-deposition thermal treatments (labeled as TT) in air as a function of the annealing temperature. The spectra are vertically shifted for better clarity.
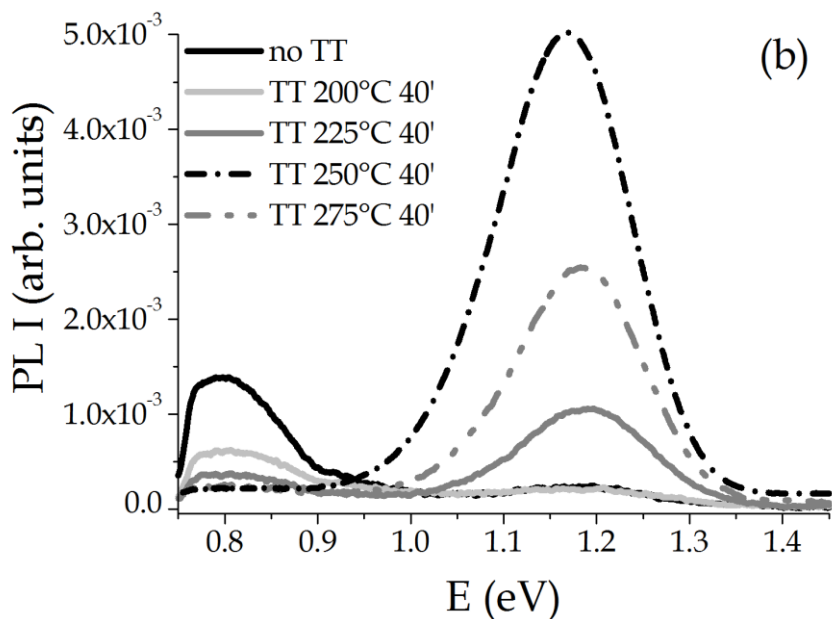
Figure 8. (a) PL spectra at 14 K before any thermal treatment (labeled as TT) (black line λ_{exc}= 805 nm, grey line λ_{exc}= 532 nm); (b) PL spectra at 14 K before and after 40 min post-deposition thermal treatments (labeled as TT) in air as a function of the annealing temperature (λ_{exc}= 805 nm).
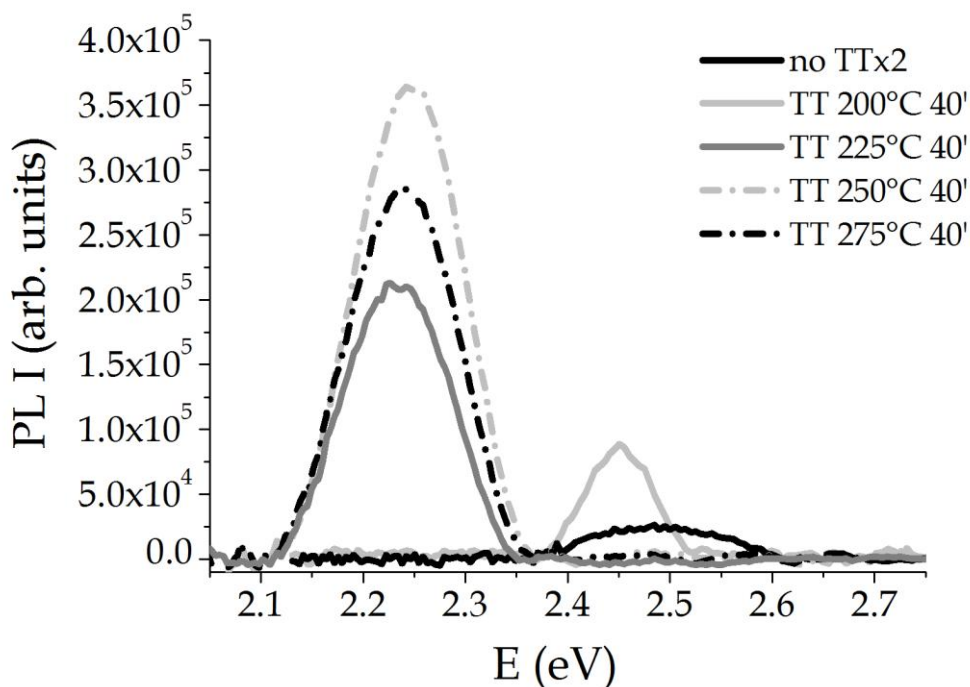

Figure 9. PL spectra at 7 K before and after 40 min post-deposition thermal treatments (labeled as TT) in air as a function of the annealing temperature (λ_{exc}= 400 nm).